Nanoscale

PAPER

View Article Online
View Journal | View Issue

Cite this: *Nanoscale*, 2022, **14**, 7314

Nonmonotonic wavelength dependence of the polarization-sensitive infrared photoresponse of an anisotropic semimetal†

Jie Deng,‡[a,b] Wei Zhang,‡[c] Xu Dai,[a,b] Yu Yu,[a] Zhifeng Li,[a,b] Wei Wang,[c] Lin Wang,*[c] Jing Zhou*[a,b] and Xiaoshuang Chen*[a,b]

Layered semimetals with in-plane anisotropy are promising for advanced polarization-sensitive infrared detection. The investigation of the polarization-dependent photoresponse of semimetals over the whole visible-to-long-wave-infrared range and revealing the physical connection between their optoelectronic properties, optical properties, and electronic band structures is required, but there have been very few studies of this kind. In this work, we conducted a thorough investigation on the polarization-dependent infrared photoresponse of WTe_2 over the visible-to-long-wave-infrared range and discovered a textbook-like perfect consistency between the wavelength-dependent polarization-sensitive photoresponse and the anisotropic dielectric constant mainly affected by interband transitions near the Weyl point. It is revealed that the polarization sensitivity and the responsivity both vary non-monotonically with the wavelength. This phenomenon is attributed to the polarization selective excitation of interband transitions associated with asymmetrically distributed electron orbitals around the Weyl points. Concerning the infrared detection properties of WTe_2, a maximum responsivity of 0.68 mA W^{-1} is obtained under self-powered operation. The power dependence of the photoresponse is linear, and the response time is around 14 μs. This work would provoke further studies about the anisotropic photoresponse associated with the transitions even closer to the Dirac or Weyl points, and it provides an approach to select the right semimetal for the right wavelength range of infrared polarization detection.

Received 16th December 2021,
Accepted 21st March 2022

DOI: 10.1039/d1nr08268j

rsc.li/nanoscale

Introduction

Polarization-sensitive infrared detection plays a critical role in many important fields, including remote sensing, optical communication, and astronomy.[1] The essential part of this technology is polarization discriminative infrared detectors. Although considerable polarization selectivity can be achieved by integrating anisotropic photonic structures with detection materials,[2–7] the fabrication of these composite structures is sophisticated and costly. Recently, the emergence of low-symmetry layered materials has stimulated tremendous research interest in polarization detection based on their in-plane anisotropic optical and electrical properties.[8–11] Among these low-symmetry 2D materials, narrow-gap candidates such as BP,[12] Te,[13,14] and GeAs[15] have been proposed for polarization detection within the visible-to-short-wave infrared range. Polarization detection at even longer wavelengths requires active materials with narrower band gaps. The extreme case of narrowing down the gap ends up with gapless semimetals. Semimetals have been demonstrated to be promising for infrared detection at room temperature due to their gapless electronic structures, unique carrier transportation characteristics, and nonlinear high responsivities at the Dirac or Weyl points.[16–20] Especially, low-symmetry semimetals with anisotropic optoelectronic properties, such as $MoTe_2$,[17] $TaIrTe_4$,[18,19] and $PtTe_2$ [20] have been revealed to be polarization sensitive to infrared light. In this sense, it is extremely important to investigate the polarization-dependent photoresponses of polarization-infrared-detection candidate materials over the whole visible-to-long-wave-infrared range and reveal the physical connection between their optoelectronic properties, optical properties, and electronic band structures. However, there have been very few studies of this kind.

In this work, we conducted a thorough investigation on the polarization-dependent infrared photoresponse of WTe_2 over the visible-to-long-wave-infrared range and discovered a

[a]State Key Laboratory of Infrared Physics, Shanghai Institute of Technical Physics, Chinese Academy of Sciences, Shanghai 200083, China.
E-mail: jzhou@mail.sitp.ac.cn, xschen@mail.sitp.ac.cn
[b]University of Chinese Academy of Sciences, Beijing 100049, China
[c]Key Laboratory of Flexible Electronics & Institute of Advanced Materials, Nanjing Tech University, Nanjing 211816, China. E-mail: iamlwang@njtech.edu.cn

†Electronic supplementary information (ESI) available. See DOI: https://doi.org/10.1039/d1nr08268j

‡These authors contributed equally to this work.

textbook-like perfect consistency between the wavelength-dependent polarization-sensitive photoresponse and the anisotropic dielectric constant mainly affected by the interband transitions near the Weyl point. WTe_2, as a type-II Weyl semimetal, has received much attention due to its unique electronic, magnetic, and ferroelectric properties mostly stemming from the topological singularity near the Weyl points.[21–28] In addition, since WTe_2 exhibits intrinsic in-plane anisotropy in optical and electronic properties,[29–33] it has been proposed for infrared polarization detection. We first revealed that the polarization-sensitive photoresponse of WTe_2 has a nonmonotonic wavelength dependence. The photoresponse of WTe_2 is isotropic in the visible range. The anisotropy increases with the wavelength in the near-infrared range and reaches a maximum of 2.3 at a wavelength of around 1.55 μm. After that, it decays with the wavelength and disappears at a wavelength of 10 μm. It is noteworthy that we designed two forms of electrodes to exclude the edge effect at the metal contacts. The nonmonotonic wavelength dependence of the polarization-sensitive photoresponse is highly consistent with the wavelength-dependent anisotropic dielectric constant of WTe_2. In addition, the responsivity also shows a nonmonotonic wavelength dependence. It forms a peak in the short-to-long-wave-infrared regime. The summit at a wavelength of 8 μm is several to ten times higher than the responsivities at the wavelengths shorter than 6.5 μm or longer than 10 μm. The nonmonotonic behavior is attributed to the joint effect of the asymmetric distribution of electron orbitals and the selection rules of the interband transitions around the Weyl points.

Results and discussion

As shown in Fig. 1(a), the crystal structure of T_d-WTe_2 is orthorhombic, non-centrosymmetric, and is in the space group $Pmn2_1$ (C_{2v}). The T_d-phase of WTe_2 is the stable form with minimum energy configuration.[34,35] Each layer of the structure consists of a single sheet of tungsten atoms sandwiched by two sheets of tellurium atoms. The quasi-1D W–W chain is along the *a*-axis and the *c*-axis is perpendicular to these layers. There are two tungsten atoms and four tellurium atoms in a unit cell. The T_d phase of our WTe_2 is proved by Raman spectroscopy. As shown in Fig. 1(b), the peaks at the wavenumbers of 80, 117, 133, 164, and 212 cm^{-1} are the features of the A_1 phonon mode.[33] T_d-WTe_2 is known as a type-II Weyl semimetal candidate and has received broad attention due to its unique optoelectronic properties. The anisotropic orthorhombic crystal structure of T_d-WTe_2 induces a highly anisotropic band structure, Fermi surface, and effective carrier mass, leading to polarization-sensitive optoelectronic properties. Polarization-resolved Raman spectroscopy was used to determine the crystallographic orientation of WTe_2. The Raman intensity peak at 212 cm^{-1} is associated with the vibration of W atoms along the *c*-axis, and it drops to a minimum when the incident light polarization is parallel to the *a*-axis. As shown in Fig. 1(c), the minimum intensity appears at 0°, indicating that the *a*-axis of the sample in Fig. 1(d) is horizontal.

Optoelectronic characterization was performed by connecting a piece of WTe_2 with two metal contacts. Metal electrodes made of Ti (10 nm)/Au (35 nm) were fabricated on a SiO_2 (300 nm)/Si substrate. Then, the as-exfoliated WTe_2 flakes were

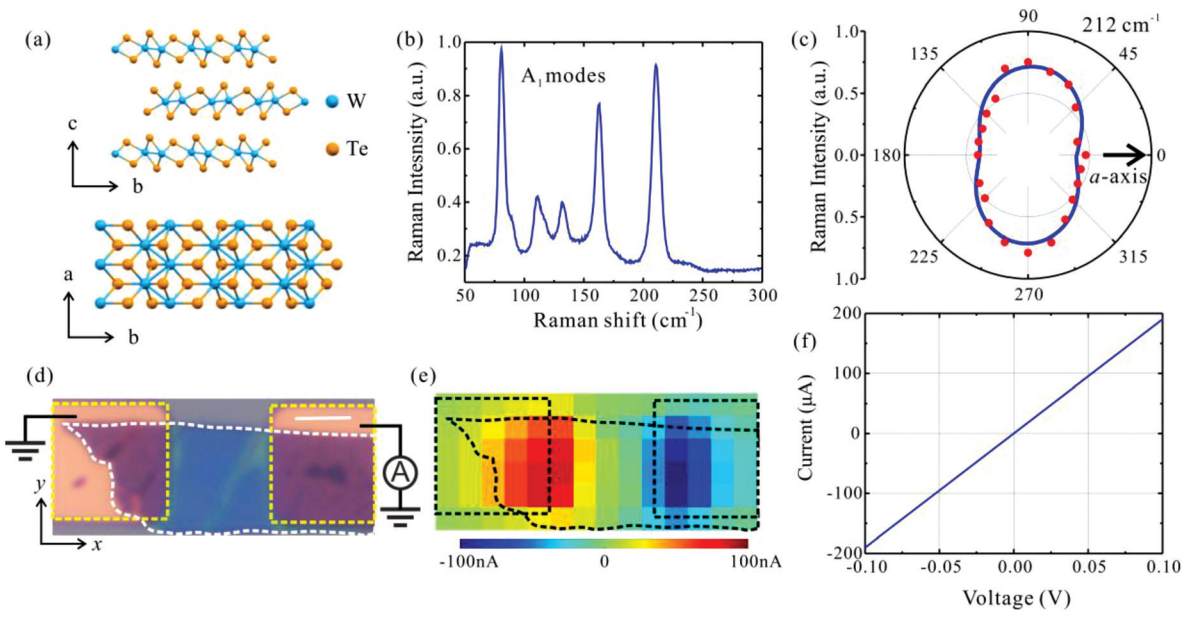

Fig. 1 (a) Side and top views of the crystal structure of T_d-WTe_2. Orange spheres: tellurium (Te) atoms and blue spheres: tungsten (W) atoms. (b) Raman spectrum of T_d-WTe_2 flakes under 532 nm laser excitation. (c) Polarization dependence of the Raman intensities at a wavenumber of 212 cm^{-1}. An arrow indicates that the *a*-axis is along the 0° direction. (d) Microscopic image of a WTe_2 device. The scale bar is 5 μm. (e) Spatially resolved photocurrent mapping of the device in (d) using a 519 nm laser. (f) *I*–*V* characteristic of the device in (d).

transferred onto the electrodes in a designed orientation. The thicknesses of the WTe_2 flakes in our devices are about 11–15 nm. A typical metal–WTe_2–metal structure is displayed in Fig. 1(d). The *a*-axis of the WTe_2 flakes is aligned parallel to the channel. Since the WTe_2 flakes are semimetallic, an ohmic contact is realized without extra metalization. According to the *I–V* test, the resistance of the device is around 500 Ω (Fig. 1(f)). A homemade spatially resolved photocurrent mapping system was used to characterize the photocurrent distribution. The spatial resolution is about 1 μm when the wavelength of the excitation light is 519 nm.

As shown in Fig. 1(e), the WTe_2 flakes and electrodes are indicated by dashed lines. At zero bias, most photocurrent is collected in the vicinity of metal contacts. WTe_2 in the middle of the channel contributes very little to the photocurrent. In the absence of an external bias, the photoresponse is attributed to the photovoltaic (PV) or the photo-thermoelectric (PTE) effect.[36] The work function difference between the metal contact and the WTe_2 flakes create a space charge region, where the electronic band is bent. The PV effect comes from the built-in electric field that separates photoexcited electron–hole pairs. The PTE effect comes from the difference of the Seebeck coefficients between the WTe_2 on the metal contact and that on the substrate, and the temperature gradient excited by a focused laser spot.

The polarization-sensitive infrared photoresponse of WTe_2 is investigated using a homemade polarization-resolved infrared optoelectronic characterization system, as shown in Fig. 2(a). The polarization state of the incident light is controlled by a linear polarizer and a half-wave plate. The polarization angle θ is defined as the angle between the electric field of the incident light and the *x*-axis. For visible and near-infrared light, the focused laser spot is smaller than 2.5 μm in diameter. The mid-infrared light spots are about 35, 45, 55, and 65 μm in diameter for wavelengths of 4.75, 6.7, 8, and 10 μm, respectively. As shown in Fig. 2(b), the electrodes of Device1 are parallel to the *a*-axis of WTe_2, and the electrodes of Device2 are perpendicular to the *a*-axis. The relative orientation between the electrodes and WTe_2 is arranged in two orthogonal forms for these two devices to eliminate the influence of metal contacts on the photoresponse anisotropy. It has been reported that polarization selective photoresponse occurs at the junctions of isotropic 2D materials and metal contacts due to photovoltaic effects and surface plasmon excitation.[37] The two devices have similar resistances (450–500 Ω). For each device, the photocurrent was collected by focusing the laser spot at a WTe_2–metal junction. The photoresponse anisotropy can be quantified by the degree of linear polarization (DOLP). The DOLP is defined as $(I_{90} - I_0)/(I_{90} + I_0)$, where $I_{0°}$ or $I_{90°}$ denotes the photocurrent induced by the incident light polarized along the *x*-axis (*i.e.* $\theta = 0°$) or the *y*-axis (*i.e.* $\theta = 90°$). Fig. 2(c) presents the wavelength-dependent DOLP for these two devices. The absolute values of $DOLP_1$ and $DOLP_2$ are almost equal to each other, indicating a similar wavelength dependence of the two devices. Regardless of the relative orientation between the incident polarization and the electrodes, the incident polarization along the *a*-axis induces a larger photocurrent than that along the *b*-axis in certain wavelength ranges. Thus, the geometric edge effect at the metal contacts is ruled out, and we conclude that the polarization selective photoresponse originates from the anisotropic optoelectronic properties of WTe_2. The DOLP of WTe_2 is tiny in the visible range, and then it increases in the near-infrared range. After the climax as high as 0.4 at a wavelength of around 1.55 μm, the DOLP decreases with the increasing wavelength and almost vanishes at the wavelengths longer than 6.7 μm. The

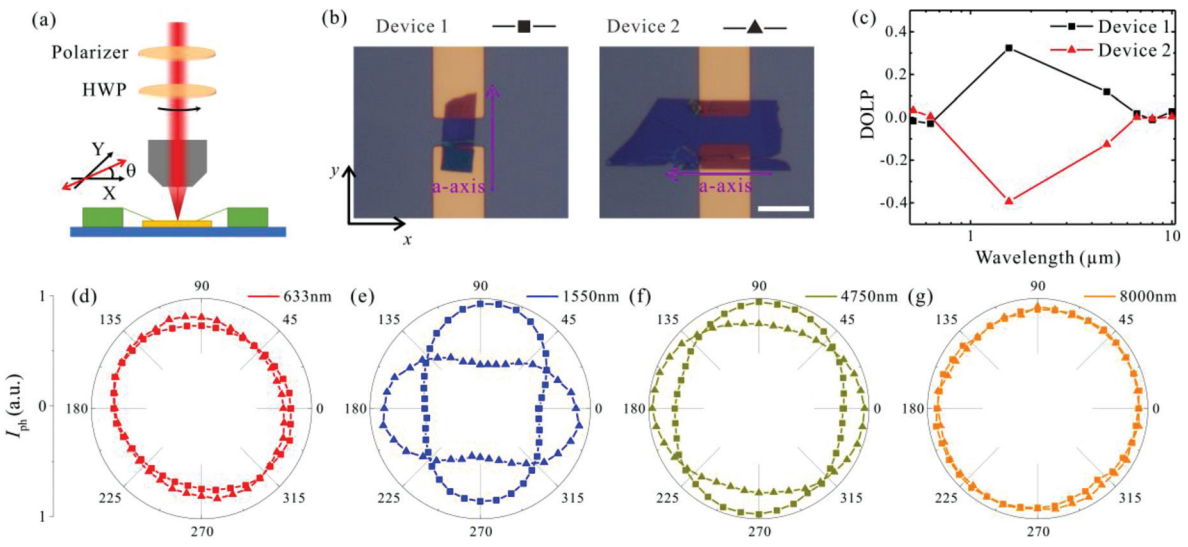

Fig. 2 (a) Schematic of the polarization-resolved infrared optoelectronic characterization setup. (b) Microscopic image of the two metal–WTe_2–metal devices. The electrodes of Device1 are parallel to the *a*-axis of WTe_2, and the electrodes of Device2 are perpendicular to the *a*-axis. The scale bar is 10 μm. (c) The DOLP of the photocurrents of Device1 and 2. (d)–(g) Polarization-dependent photocurrents for the linear-polarized excitations at 633 nm, 1550 nm, 4.75 μm, and 8 μm, respectively. The square symbols correspond to Device1, and the triangle symbols correspond to Device2.

wavelength-dependent evolution of the anisotropic photocurrent is further illustrated at four wavelengths. Fig. 2(d)–(g) show the polarization-dependent photoresponses of these two devices at the wavelengths of 633 nm, 1550 nm, 4.75 μm, and 8 μm, respectively. The square symbols correspond to Device1 and the triangle symbols correspond to Device2.

The wavelength-dependent polarization-sensitive photoresponses of our devices are consistent with the dielectric constant spectra extracted from reflection measurements[38] or predicted by first-principle calculations.[31,32,38] Fig. 3(a) shows the real part of optical conductivity $Re(\sigma) = Re(-2\pi i\omega[\varepsilon(\omega) - \varepsilon_\infty]/Z_0)$ (where $Z_0 \approx 377\ \Omega$) derived from the dielectric constant.[38] The optical conductivity is directly associated with the optical response of the material. σ_a or σ_b denotes the optical conductivity along the *a*- or *b*-axis. The optical properties of WTe_2 have free-carrier response in the low energy domain ($h\nu <$ ~60 meV), interband transitions near the Weyl points (~0.2 eV < $h\nu$ < ~0.8 eV), and interband transitions to higher energy levels ($h\nu >$ ~0.8 eV).[38–41] Our investigation covers the photon energy range from 0.1 to 2.4 eV. In the range from 0.1 to 0.2 eV, the photon energies are not high enough to excite interband transitions, but still too high to excite prominent free-carrier response. Thus, the light absorption of WTe_2 in this range is pretty low no matter whether the polarization is along the *a*-axis or the *b*-axis. As a result, the polarization extinction ratio (PER), defined as I_a/I_b, is around 1 (Fig. 3(b)). In the range from 0.2 to 0.8 eV, the light–WTe_2 interaction is determined by transitions near the Weyl points since the interband transitions at other positions in the *k*-space require much higher photon energies.[31,32,41] In this range, either σ_a or σ_b increases almost linearly with the photon energy, which is a featured consequence of linear band structures near the Weyl points.[38,40,41] σ_a and σ_b increase at different rates with the photon energy, as shown in Fig. 3(b), so the in-plane anisotropy of the photoresponse grows with the photon energy and reaches a maximum at 0.8 eV. The polarization selective excitation of these interband transitions is probably attributed to the asymmetric distribution of electron orbitals around the Weyl points, as predicted by theories.[31,32,41] In principle, the crystal symmetry of T_d-WTe_2 forbids more transitions associated with the polarization along the *b*-axis than along the *a*-axis due to the selection rule. These transitions are not directly at the Weyl points, since the direct transitions between the upper and lower Weyl cones are expected to occur at even lower energy regimes, overlapping the free carrier response range.

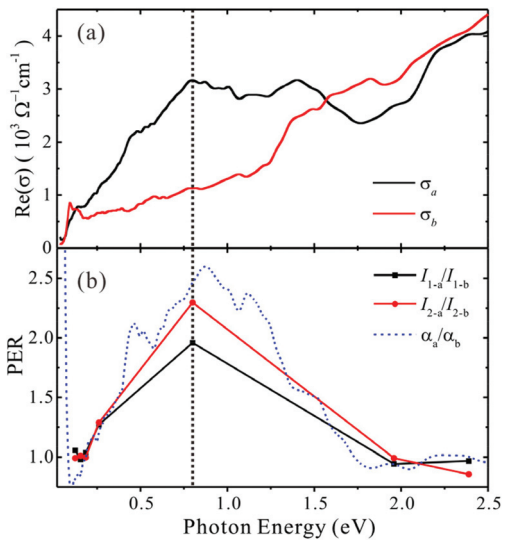

Fig. 3 (a) Optical conductivities of WTe_2 along the *a*-axis and the *b*-axis, respectively, based on the dielectric function from ref. 38. (b) Polarization extinction ratio spectra of the two devices. The square and triangle symbols correspond to Device1 and Device2, respectively. The dashed blue line denotes the ratio of the absorption coefficient along the *a*-axis to that along the *b*-axis.

For photon energies higher than 0.8 eV, electrons are excited to higher energy levels, and the transitions are not limited to the *k*-space near the Weyl points but distributed more widely over the whole *k*-space. As a result, there are more possibilities for the transitions associated with the polarization along the *b*-axis. As confirmed by our experiment, the PER decreases with the photon energy after 0.8 eV and finally goes back to 1 (Fig. 3(b)).

The nonmonotonic wavelength dependence of the photoresponse PER is different from the findings in previous studies on anisotropic semimetals, such as $MoTe_2$, $TaIrTe_4$, and $PtTe_2$.[17–20] Each of these studies measured the polarization-dependent photoresponse at 3 or 4 wavelengths in the visible-to-long-wave-infrared range. All the results indicate that the photoresponse PERs increase with the wavelength monotonically. This phenomenon was attributed to the anisotropic effective masses of carriers and anisotropic absorption along the two principal axes. However, the discussions on that were very brief, and the wavelength-dependent anisotropic photoresponses were not compared with the spectra of light absorption or dielectric constants. In our study, we measured the polarization-dependent photoresponse at 7 wavelengths more evenly distributed in the visible-to-long-wavelength-infrared range and analyzed the results with the spectra of the anisotropic optical conductivities and absorption coefficients. Based on the consistency between the anisotropic photoresponses and the anisotropic optical properties, we confirm that the photoresponse anisotropy of WTe_2 has a nonmonotonic wavelength dependence in the visible-to-long-wave-infrared range, and the highest PER occurs around a wavelength of 1.55 μm. As reported by a previous study,[42] WTe_2 can have prominent polarization-sensitive photoresponse in the visible range because the incident light polarized along the *a*-axis can open a bandgap to induce extra interband transitions, while the light polarized along the *b*-axis cannot. Probably due to the low intensity of our laser, we did not observe a polarization-sensitive photoresponse of our WTe_2 in the visible range.

As shown in Fig. 4(a), photocurrent waveforms at different incident wavelengths are recorded by using a digital source meter. The photocurrent is collected by focusing the laser spot at a WTe_2–metal junction under zero bias. The responsivities at the wavelengths of 519 nm, 633 nm, 1550 nm, 4.75 μm,

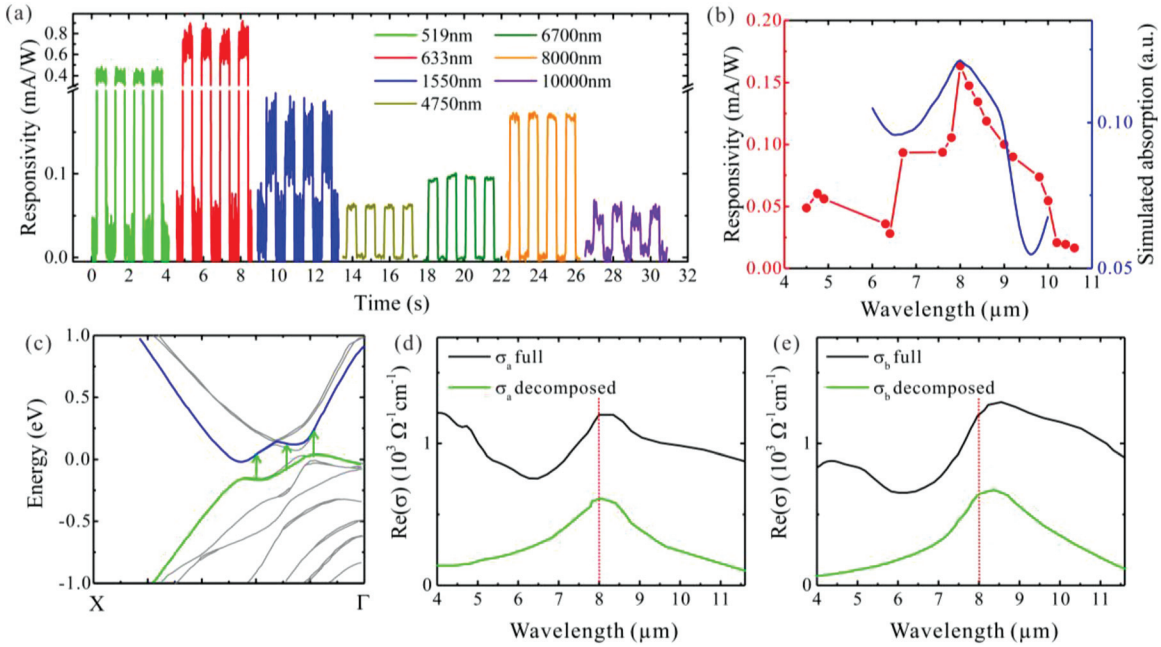

Fig. 4 (a) Photoresponse waveforms of WTe_2 over the visible-to-long-wave-infrared range. (b) Responsivity spectrum (red) and simulated absorption spectrum (blue) in the mid-infrared range. (c) Electronic band structure of WTe_2 along the Γ–X direction based on first-principle calculations. The data are reproduced from ref. 38. (d) and (e) Optical conductivity spectrum (black line) of WTe_2 along the *a*-axis (σ_a) or the *b*-axis (σ_b), and the decomposed σ_a or σ_b spectrum (green line) for the specific interband transition marked by the green arrows in (c).

6.7 μm, 8 μm, and 10 μm are 0.4 mA W^{-1}, 0.68 mA W^{-1}, 0.14 mA W^{-1}, 60 μA W^{-1}, 93 μA W^{-1}, 163 μA W^{-1}, and 54 μA W^{-1} respectively. The responsivities in the visible-to-near-infrared range are 2.5 times to 4.5 times higher than those in the mid-infrared range since the visible photons with higher energies can excite more interband transitions. The responsivity level of our WTe_2 devices is similar to reported values for other semimetals.[17–20] It is worth noting that in the mid-infrared range the responsivity of WTe_2 increases with the wavelength initially, climaxes at a wavelength of 8 μm, and decreases after that (Fig. 4(b)). The maximum responsivity at the wavelength of 8 μm is 10 times higher than the minimum responsivity at a wavelength of 10.6 μm. The responsivity peak wavelength coincides with the optical conductivity peak wavelength, as shown in Fig. 4(d) and (e). According to the interband conductivity decomposition,[38] the peak at the wavelength of 8 μm is attributed to the interband transition near the Weyl points, as indicated by the green arrows in Fig. 4(c). This transition starts from the band drawn in green and ends at the band in blue. The decomposed conductivities for this specific transition along the *a*-axis and that along the *b*-axis are plotted in green lines in Fig. 4(d) and (e), respectively. Both of them show a distinct peak around the wavelength of 8 μm, indicating that this transition can be excited by either the polarization along the *a*-axis or that along the *b*-axis. A simulation using this optical conductivity was also performed to investigate the absorption of WTe_2 on a SiO_2/Si substrate. As shown by the blue line in Fig. 4(b), the absorptance peak at the wavelength of 8 μm is consistent with the responsivity peak at the same wavelength.

In addition to interband transitions, WTe_2, as a semimetal, has also free-carrier response. However, since the free-carrier response typically follows a Drude behavior, it has no peak features in the spectrum.

Concerning the infrared detection properties of WTe_2, the power dependence of the photoresponse is also studied over the visible-to-long-wave-infrared range. Fig. 5(a) shows the

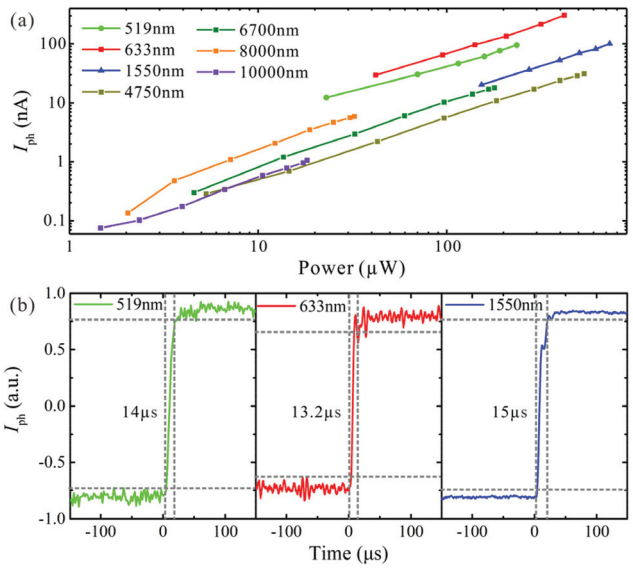

Fig. 5 (a) Power-dependent photocurrents of WTe_2. (b) Time-resolved photoresponses of WTe_2.

photocurrent as a function of excitation power. The photocurrents grow linearly with the incident power, indicating that the carriers experience a low density of trap states during transportation.[43] The photoresponse time was characterized by using an oscilloscope. Based on the waveforms (Fig. 5(b)) recorded by the oscilloscope, the photoresponse time is around 14 μs.

Conclusions

The polarization-sensitive photoresponse spectroscopy of WTe_2 was studied over the visible-to-long-wave-infrared range. It is revealed that the polarization sensitivity of the photoresponse varies non-monotonically with the wavelength, which is different from previous findings on other semimetals. The photoresponse of WTe_2 is almost polarization-independent in the visible range. The PER increases with the wavelength in the near-infrared range and reaches a maximum of 2.3 at a wavelength of around 1.55 μm. Then, it decays with the wavelength in the near-to-long-wave-infrared range and degenerates to ~1 at a wavelength of 10 μm. The employment of two devices with orthogonal electrodes-WTe_2 relative orientations (*i.e.* electrodes along the *a*-axis and electrodes along the *b*-axis) proves that the polarization-sensitive photoresponse is an intrinsic property of the WTe_2 material. The nonmonotonic wavelength-dependent anisotropy is attributed to the polarization selective excitation of interband transitions associated with asymmetrically distributed electron orbitals around the Weyl points, and it is highly consistent with the wavelength-dependent anisotropic dielectric constant of WTe_2. In addition, the responsivity also varies non-monotonically with the wavelength. It shows a peak of 163 μA W^{-1} at a wavelength of 8 μm in the mid-infrared range. This phenomenon is attributed to a specific interband transition with a higher rate near the Weyl points. A maximum responsivity of 0.68 mA W^{-1} is obtained under zero bias. The power dependence of the photoresponse is linear, and the response time is around 14 μs. This work would provoke further studies about the anisotropic photoresponse of topological semimetals associated with the transitions even closer to the Dirac or Weyl points. It also indicates that the polarization-dependent photoresponse of a semimetal is mainly decided by its anisotropic dielectric constant, so the right material for the right wavelength range can be selected for polarization infrared detection simply based on the dielectric constant.

Experimental section

Sample growth

The WTe_2 crystals studied in this work were synthesized by the chemical vapor transportation (CVT) method.[28] The WTe_2 crystals were mechanically exfoliated into nanosheets using Scotch tape.

Device fabrication

The devices were fabricated by standard UV lithography, electron beam deposition, and the lift-off process. The metal electrodes were made of Ti (10 nm)/Au (35 nm). The as-exfoliated WTe_2 flakes were transferred onto the electrodes by a dry-transfer technique. The thicknesses of the WTe_2 flakes were measured by atomic force microscopy (Fig. S1†).

Photoelectric characterization

All of the electronic and optoelectronic properties were measured under ambient conditions at room temperature. The *I–V* curves and waveforms were recorded by using a source meter (Agilent B2912A). After being converted to a voltage signal by a current preamplifier (Stanford Research Systems SR570), the time-resolved photoresponse was recorded using an oscilloscope. For polarization- and power-dependent measurements, the incident light was modulated at 333 Hz, and the photoresponse was recorded using a lock-in amplifier (Stanford Research Systems SR830) after the current preamplifier. For linear polarization measurements, a half-wave plate was placed after the linear polarizer to control the polarization of incident light. The incident power was characterized using a power meter.

For the visible and the near-infrared photoresponse measurements, the light from a single-mode pigtailed laser diode (Thorlabs) was focused on the sample by a 50× objective lens. The light spot size is smaller than 2.5 μm. The light power was modulated using a signal generator *via* a laser diode driver. For the mid-infrared photoresponse measurements, a quantum cascade laser with multiple chips was employed. A 15× reflective objective was used to focus the laser beam. The light power was modulated with a mechanical chopper or an electronic shutter. The diameter of the light spots is about 35, 45, 55, and 65 μm for the wavelengths of 4.75, 6.7, 8, and 10 μm, respectively, and the power is 6.3, 4.1, 1.2, and 1.2 mW for the wavelengths of 4.75, 6.7, 8, and 10 μm, respectively. The accurate positioning of the infrared light spot on the sample was assisted by a visible laser which has been aligned with the infrared light.

Conflicts of interest

There are no conflicts to declare.

Acknowledgements

This work was supported by the National Key Research and Development Program of China (2017YFA0205800, 2018YFA0306200, and 2020YFA0308900); the National Natural Science Foundation of China (61975223, 91850208, 61991442, 61521005, 92064010, and 61874126); the Hundred Talents Program of the Chinese Academy of Sciences (No. 20181214); the Key Deployment Projects of the Chinese Academy of Sciences (ZDRW-XH-2021-7-1); the Shanghai Municipal

Science and Technology Major Project (Grant No. 2019SHZDZX01); the ShanghaiTech University Quantum Device Lab (SQDL); and the Open Project of the State Key Laboratory of Infrared Physics (M202004). The authors acknowledge the support from Zheng Fan and Zhaoxin Zhu from SQDL on fabrication.

References

1 J. P. Brown, M. C. Wagner, R. G. Roberts and D. B. Card, *Proc. SPIE*, 2019, **11001**, 1100107.
2 S. Guo, D. Zhang, J. Zhou, J. Deng, Y. Yu, J. Deng, Q. Cai, Z. Li, W. Lu and X. Chen, *Carbon*, 2020, **170**, 49–58.
3 J. Deng, Y. Zheng, J. Zhou, Z. Li, S. Guo, X. Dai, Y. Yu, Z. Ji, Z. Chu, X. Chen and W. Lu, *Opt. Express*, 2020, **28**, 16427.
4 D. Zhang, J. Zhou, C. Liu, S. Guo, J. Deng, Q. Cai, Z. Li, Y. Zhang, W. Zhang and X. Chen, *J. Appl. Phys.*, 2019, **126**, 074301.
5 Z. Chu, J. Zhou, X. Dai, F. Li, M. Lan, Z. Ji, W. Lu and X. Chen, *Adv. Opt. Mater.*, 2020, **8**, 1901800.
6 J. Zhou, J. Deng, M. Shi, Z. Chu, H. Li, R. Dong and X. Chen, *Appl. Phys. Lett.*, 2021, **119**, 160504.
7 L. Huang, G. Li, A. Gurarslan, Y. Yu, R. Kirste, W. Guo, J. Zhao, R. Collazo, Z. Sitar, G. N. Parsons, M. Kudenov and L. Cao, *ACS Nano*, 2016, **10**, 7493–7499.
8 S. Zhao, B. Dong, H. Wang, H. Wang, Y. Zhang, Z. V. Han and H. Zhang, *Nanoscale Adv.*, 2020, **2**, 109–139.
9 L. Li, W. Han, L. Pi, P. Niu, J. Han, C. Wang, B. Su, H. Li, J. Xiong, Y. Bando and T. Zhai, *InfoMat*, 2019, **1**, 54–73.
10 Y. Fang, Y. Ge, C. Wang and H. Zhang, *Laser Photonics Rev.*, 2020, **14**, 1900098.
11 T. Tan, X. Jiang, C. Wang, B. Yao and H. Zhang, *Adv. Sci.*, 2020, **7**, 2000058.
12 H. Yuan, X. Liu, F. Afshinmanesh, W. Li, G. Xu, J. Sun, B. Lian, A. G. Curto, G. Ye, Y. Hikita, Z. Shen, S.-C. Zhang, X. Chen, M. Brongersma, H. Y. Hwang and Y. Cui, *Nat. Nanotechnol.*, 2015, **10**, 707–713.
13 L. Tong, X. Huang, P. Wang, L. Ye, M. Peng, L. An, Q. Sun, Y. Zhang, G. Yang, Z. Li, F. Zhong, F. Wang, Y. Wang, M. Motlag, W. Wu, G. J. Cheng and W. Hu, *Nat. Commun.*, 2020, **11**, 2308.
14 M. Amani, C. Tan, G. Zhang, C. Zhao, J. Bullock, X. Song, H. Kim, V. R. Shrestha, Y. Gao, K. B. Crozier, M. Scott and A. Javey, *ACS Nano*, 2018, **12**, 7253–7263.
15 Z. Zhou, M. Long, L. Pan, X. Wang, M. Zhong, M. Blei, J. Wang, J. Fang, S. Tongay, W. Hu, J. Li and Z. Wei, *ACS Nano*, 2018, **12**, 12416–12423.
16 J. Liu, F. Xia, D. Xiao, F. J. García de Abajo and D. Sun, *Nat. Mater.*, 2020, **19**, 830–837.
17 J. Lai, X. Liu, J. Ma, Q. Wang, K. Zhang, X. Ren, Y. Liu, Q. Gu, X. Zhuo, W. Lu, Y. Wu, Y. Li, J. Feng, S. Zhou, J.-H. Chen and D. Sun, *Adv. Mater.*, 2018, **30**, 1707152.
18 J. Lai, Y. Liu, J. Ma, X. Zhuo, Y. Peng, W. Lu, Z. Liu, J. Chen and D. Sun, *ACS Nano*, 2018, **12**, 4055–4061.
19 X. Zhuo, J. Lai, P. Yu, Z. Yu, J. Ma, W. Lu, M. Liu, Z. Liu and D. Sun, *Light: Sci. Appl.*, 2021, **10**, 101.
20 T. Wei, X. Wang, Q. Yang, Z. He, P. Yu, Z. Xie, H. Chen, S. Li and S. Wu, *ACS Appl. Mater. Interfaces*, 2021, **13**, 22757–22764.
21 M. N. Ali, J. Xiong, S. Flynn, J. Tao, Q. D. Gibson, L. M. Schoop, T. Liang, N. Haldolaarachchige, M. Hirschberger, N. P. Ong and R. J. Cava, *Nature*, 2014, **514**, 205–208.
22 E. Sajadi, T. Palomaki, Z. Fei, W. Zhao, P. Bement, C. Olsen, S. Luescher, X. Xu, J. A. Folk and D. H. Cobden, *Science*, 2018, **362**, 922–925.
23 P. Sharma, F.-X. Xiang, D.-F. Shao, D. Zhang, E. Y. Tsymbal, A. R. Hamilton and J. Seidel, *Sci. Adv.*, 2019, **5**, eaax5080.
24 Z. Fei, T. Palomaki, S. Wu, W. Zhao, X. Cai, B. Sun, P. Nguyen, J. Finney, X. Xu and D. H. Cobden, *Nat. Phys.*, 2017, **13**, 677–682.
25 Q. Wang, J. Zheng, Y. He, J. Cao, X. Liu, M. Wang, J. Ma, J. Lai, H. Lu, S. Jia, D. Yan, Y. Shi, J. Duan, J. Han, W. Xiao, J.-H. Chen, K. Sun, Y. Yao and D. Sun, *Nat. Commun.*, 2019, **10**, 5736.
26 Y.-B. Choi, Y. Xie, C.-Z. Chen, J. Park, S.-B. Song, J. Yoon, B. J. Kim, T. Taniguchi, K. Watanabe, J. Kim, K. C. Fong, M. N. Ali, K. T. Law and G.-H. Lee, *Nat. Mater.*, 2020, **19**, 974–979.
27 C. Wang, S. Huang, Q. Xing, Y. Xie, C. Song, F. Wang and H. Yan, *Nat. Commun.*, 2020, **11**, 1158.
28 L. Wang, I. Gutiérrez-Lezama, C. Barreteau, N. Ubrig, E. Giannini and A. F. Morpurgo, *Nat. Commun.*, 2015, **6**, 8892.
29 Q. Wang, C. Yesilyurt, F. Liu, Z. B. Siu, K. Cai, D. Kumar, Z. Liu, M. B. A. Jalil and H. Yang, *Nano Lett.*, 2019, **19**, 2647–2652.
30 Q. Zhang, R. Zhang, J. Chen, W. Shen, C. An, X. Hu, M. Dong, J. Liu and L. Zhu, *Beilstein J. Nanotechnol.*, 2019, **10**, 1745–1753.
31 A. Popescu, A. Pertsova, A. V. Balatsky and L. M. Woods, *Adv. Theory Simul.*, 2020, **3**, 1900247.
32 E. Torun, H. Sahin, S. Cahangirov, A. Rubio and F. M. Peeters, *J. Appl. Phys.*, 2016, **119**, 074307.
33 Q. Song, X. Pan, H. Wang, K. Zhang, Q. Tan, P. Li, Y. Wan, Y. Wang, X. Xu, M. Lin, X. Wan, F. Song and L. Dai, *Sci. Rep.*, 2016, **6**, 29254.
34 J. A. Wilson and A. D. Yoffe, *Adv. Phys.*, 1969, **18**, 193–335.
35 B. E. Brown, *Acta Crystallogr.*, 1966, **20**, 268–274.
36 F. H. L. Koppens, T. Mueller, Ph. Avouris, A. C. Ferrari, M. S. Vitiello and M. Polini, *Nat. Nanotechnol.*, 2014, **9**, 780–793.
37 T. Hong, B. Chamlagain, S. Hu, S. M. Weiss, Z. Zhou and Y.-Q. Xu, *ACS Nano*, 2015, **9**, 5357–5363.

38 A. J. Frenzel, C. C. Homes, Q. D. Gibson, Y. M. Shao, K. W. Post, A. Charnukha, R. J. Cava and D. N. Basov, *Phys. Rev. B*, 2017, **95**, 245140.
39 S. Kimura, Y. Nakajima, Z. Mita, R. Jha, R. Higashinaka, T. D. Matsuda and Y. Aoki, *Phys. Rev. B*, 2019, **99**, 195203.
40 P. E. C. Ashby and J. P. Carbotte, *Phys. Rev. B: Condens. Matter Mater. Phys.*, 2014, **89**, 245121.
41 M.-X. Guan, E. Wang, P.-W. You, J.-T. Sun and S. Meng, *Nat. Commun.*, 2021, **12**, 1885.
42 W. Zhou, J. Chen, H. Gao, T. Hu, S. Ruan, A. Stroppa and W. Ren, *Adv. Mater.*, 2019, **31**, 1804629.
43 A. Rose, *Concepts in photoconductivity and allied problems*, Krieger, Huntington, N.Y., Rev. ed., with corrections and new material, 1978.